J. Comp. App. Res. Mech. Eng. Vol. X. No. X, pp. X-X, XXXX *DOI: 10.22061/jcarme.XXXX.XXXX.XXXX*

SRTTU

Journal of Computational and Applied Research in Mechanical Engineering

jcarme.sru.ac.ir

JCARME

ISSN: 2228-7922

Research paper

A numerical investigation of the effect of carbon monoxide electrochemical oxidation on the performance of a planar solid oxide fuel cell fuelled by synthesis gas

Mehdi Borji*

Department of Mechanical Engineering, La.C., Islamic Azad University, Lahijan, Iran.

Article info:

Article history:

Received: 00/00/00

Accepted: 00/00/00

Revised: 00/00/00

Online: 00/00/00

Keywords:

SOFC,

Synthesis gas fuelled,

Direct internal reforming,

Co electrochemical reaction,

Comprehensive numerical investigation

*** Corresponding author:**
Borji.mehdi@iau.ac.ir

Abstract

A comprehensive investigation has been conducted into the direct internal reforming planar type solid oxide fuel cell (DIR-PSOFC) through numerical analysis. The mathematical modeling of DIR-PSOFC is achieved through the implementation of conservation equations and a comprehensive electrochemical model. The synthesis gas fuel is introduced into the fuel channel, where both carbon monoxide (CO) and hydrogen (H_2) undergo electrochemical oxidation. Gas flows are treated as plug flows with a co-flow configuration. Results of the simulation are then compared with and without the inclusion of carbon monoxide electrochemical oxidation. This comparison encompasses temperature fluctuations along the cell's longitudinal axis and the mole fraction variations of all gaseous species along the cel length, in addition to the electrical performance of the SOFC. It has been demonstrated that CO accounts for only 20% of the total current density. The contribution of CO to the generation of electric current at the inlet is 15%. At the point of maximum current density, the value is 16.17%. The cell operating voltage, power density, and fuel efficiency have been demonstrated to exhibit an enhancement, with an augmentation observed from 0.68 to 0.75 V, 3411.396 to 3739.130 W/m^2, and 45.83% to 50.23%, respectively, when CO is used as a reactant in the anode side TPB. It has been determined that the electrochemical reaction of CO results in elevated heat generation within the cell, which in turn enhances the operating temperature. Consequently, the activation and ohmic losses are diminished, thereby improving the local current density and cell operating voltage.

1. Introduction

Solid oxide fuel cells (SOFCs) have been considered to be the most efficient devices yet invented for the direct conversion of chemical energy from fuels into electrical power [1]. The primary advantages of SOFCs over conventional power generation systems include high efficiency, low emissions, modularity, and the capacity to be integrated with bottoming cycles. Notably, SOFCs have the ability to utilize a diverse range of fuels, including natural gas,

propane, and syngas, due to their high operating temperature [2]. In addition to the aforementioned advantages, several disadvantages have been identified in SOFCs, including carbon deposition, thermal fracture, anode oxidation, and high cost. Indeed, the poisoning of the anode electrocatalyst by CO represents a significant concern in low operating temperature fuel cells.

At elevated operating temperatures, such as the typical operating temperature of SOFCs (800–1000°C), hydrocarbons exhibit a greater propensity to react with steam (H_2O) to form H_2 and CO than to dissociate into atomic carbon (C). Nevertheless, the possibility of carbon deposition in SOFCs remains unavoidable [3]. On the other hand, at elevated temperatures, CO can undergo oxidation with H_2O, resulting in the formation of carbon dioxide (CO_2) and H_2 under the term "Water-Gas-Shift Reaction" (WGSR). Among the various fuels that can be utilized in an SOFC, only H_2 and CO undergo electrochemical oxidation at the anode. The remaining species in the gas mixture, including methane (CH_4), are subjected to a process of reforming, resulting in the production of H_2 and/or CO. Subsequently, these reactants undergo an electrochemical reaction [4]. While the other reactions are proposed for CH_4 [5, 6], the main reaction is the Methane Steam Reforming Reaction (MSRR) for higher reaction rates.

Syngas, an acronym for synthesis gas, is a mixture of gases primarily composed of H_2, CO, CO_2, H_2O, and nitrogen (N_2). It is produced through the process of gasification, which involves the conversion of biomass and coal into gaseous form [7]. The conversion process of solid, renewable materials into combustible gas is referred to as biomass gasification. This gas can be utilized in a modern conversion device, including SOFCs. The elevated operating temperature domain of 800–1300°C is a prerequisite for the biomass gasification process [7], which has prompted considerable interest in the incorporation of SOFC with the biomass gasification process in recent years [8, 9].

Mathematical modeling and simulation have historically contributed to the comprehension of complex phenomena, particularly in the context of technological development. Consequently, in addition to some valuable experimental results [10-12], a plethora of aspects about the nonlinear character of SOFCs have been the subject of numerical investigation within the extant literature. Zero-dimensional or lumped to three-dimensional models, typically based on computational fluid dynamics (CFD) approaches, have been developed to analyze the steady-state or dynamic behavior of SOFCs [13-17]. On the other hand, there are numerous studies that have investigated the feasibility of integrating SOFCs with other cycles, such as gas turbines, gasification, and other advanced cycles [9, 18-23].

The process of converting the primary fuel into a hydrogen-rich gas mixture, which is necessary for the electrochemical reaction at the anode TPB, can be accomplished through the use of a catalytic steam reformer or a partial oxidation reactor [24]. The reforming process is carried out in the temperature range of 750–900°C [25], making it compatible with SOFCs. Different strategies have been considered, such as external, direct internal, or indirect internal reforming processes [4, 24-26]. Abdelkareem *et al.* [27] provided a comprehensive review of the processes and mechanisms that contribute to the majority of issues encountered in the operation of direct internal reforming biogas SOFCs. These issues include thermal and oxidation cycling, thermal stresses, carbon deposition, and poisoning with H_2S, siloxanes, and halides. A number of strategies have been proposed as a means of addressing these issues.

One of the products of the steam reforming reaction is CO, which is then typically converted into H_2 and CO_2 by WGSR [24, 25]. This assumption is based on the observation that the CO oxidation rates are considerably lower than those of H_2 and that the WGSR has higher reaction rates compared to the electrochemical oxidation of CO. However, some authors [5, 28-30] have investigated both H_2 and CO electrochemical reactions. Andersson *et al.* [5] have performed a numerical study with different fuel compositions. It was determined that a fuel comprising a significant proportion of H_2 and CO enables an augmented Nernst potential in the vicinity of the inlet, thereby enhancing the current density in this region. Furthermore, it was revealed that the Nernst potential associated

with the electrochemical reaction of CO is more influenced by changes in the operating temperature than that of H_2. On the other hand, studies conducted by this group have demonstrated that the H_2 electrochemical reaction is accompanied by a higher current density. Iwai *et al.*[29] have developed a quasi-three-dimensional model with a novel approach to SOFC, taking into account both CO and H_2 electrochemical reactions. The volume-averaging method was implemented to analyze the fuel and air ducts, under the assumption that a porous material was placed in the channels as a current collector. It was determined that the endothermic steam reforming reaction resulted in a decline in the local temperature in the proximity of the channel inlet, thereby constraining the rate of electrochemical reaction within this region [29]. However, the effect of the CO electrochemical oxidation has not been clearly demonstrated in this research. Minguela *et al.* [30] have carried out an energy and exergy analysis of an SOFC fuelled by four different biogas compositions derived from diverse biomass sources. A three-dimensional CFD model was employed, taking into account both CO and H_2 electrochemical reactions. The primary findings of the study pertained to the irreversibilities within the SOFC; however, the impact of the CO electrochemical reaction remained to be elucidated.

As discussed above, further investigation is necessary to adequately examine the impact of the CO electrochemical reaction on cell performance. A thorough explanation is lacking regarding the impact of CO oxidation on the electrical performance of the SOFC, the temperature field, and the distribution of gas constituents along the cell length. The objective of this study is to develop a quasi-two-dimensional model for the DIR-PSOFC, taking into account both CO and H_2 electrochemical reactions. The steam reforming reaction of methane and the water-gas shift reaction are also considered. The present study investigates the effects of the presence of CO in anodic electrochemical reactions on several key factors, including electrical power, current density, overpotentials, temperature distribution, and the mole fraction of gas constituents within the cell.

2. Mathematical model

2.1. Outline of model and assumptions

It is estimated that a standard fuel cell stack comprises numerous individual fuel cells connected in series and/or parallel to produce a useful voltage, as a single cell will barely produce enough power for even the smallest application. It is desirable to have a stack with uniformly performing cells, but the experimental results have demonstrated that the cells in a stack do not operate uniformly [31]. This reality is ignored in current work because of the complexity and computational load that will be imposed in simulations. In the case analyzed here, the focus is on a uniformly repeating single cell located in the center of a stack, so that the interactions between the favorable cells and their neighbors in a stack can be neglected. Fig. 1 schematically illustrates the configuration of an anode-supported, planar, co-flow single cell. The cell is composed of two interconnects that facilitate the flow of air and fuel and separate the cells in a stack. The core of the cell is a PEN structure, which contains a thin electrolyte sandwiched between a thin cathode and a thick anode. Even though the velocity change may be substantial within the stream ducts under both steady-state and transient conditions, the principle of conservation of linear momentum has been disregarded by numerous authors [4, 24-28, 32, 33], while other researchers consider this conservation equation in their model [5, 28, 31, 34, 35].

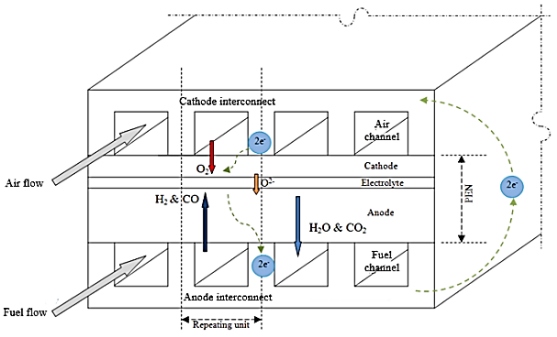

Fig. 1. Schematic representation of a single planar cell supported by anode in a co-flow configuration.

Bhattacharyya *et al.* [36] examined the effect of this assumption. It is important to acknowledge that neglecting the momentum conservation equation has the advantage of circumventing the

necessity for calculating the pressure field, thereby reducing the complexity of the solution. Accordingly, the developed model comprises the following components: four energy balances for the PEN structure, interconnect, and air and fuel channels; the principle of species mass balance for the air and fuel ducts; and a complete electrochemical model. It is widely accepted that the flow field can be modelled in a relatively straightforward manner by employing the continuity equation in the SOFC.
Furthermore, the following assumptions are considered in the simulation:

1. The fuel cell operates at steady-state.
2. It is imperative to note that the variation of the parameters along the length of the cell is the sole factor that is taken into account in this model, which is one-dimensional in nature.
3. The phenomenon of pressure drops along the channels is disregarded.
4. The gas flows are modeled as plug flows.
5. The analysis excludes the consideration of stacking effects.
6. The assumption is made that laminar flow is occurring during the process of heat transfer.
7. it is hypothesized that the WGSR is in equilibrium.
8. The radiative heat transfer between the solid structure and the gas phase is not considered.
9. Air is mainly composed of 21% oxygen and 79% nitrogen.
10. The fuel is a synthesis gas consisting of CH_4, H_2, CO, CO_2, and H_2O.
11. It is hypothesized that both the WGSR and steam reforming reactions proceed within the fuel channel.

2.2. Governing equations

2.2.1. Electrochemical model

The fuel supplied to the SOFC contains methane, which undergoes a process of reforming through Eqs. (1 and 2) [4]:

$$CH_4 + H_2O \leftrightarrows 3H_2 + CO \quad \text{(MSRR)} \qquad (1)$$

$$CO + H_2O \leftrightarrows H_2 + CO_2 \quad \text{(WGSR)} \qquad (2)$$

The kinetics of the highly endothermic MSRR and the weakly exothermic WGSR are described by first-order expressions, as illustrated in Eqs. (3 and 4) [25]:

$$\dot{r}_{MSRR} = k_0 P_{CH_4} \exp\left(-\frac{E_a}{RT}\right) \qquad (3)$$

$$\dot{r}_{WGSR} = k_{WGSR} P_{CO} \left[1 - \frac{P_{CO_2} P_{H_2} / P_{CO} P_{H_2O}}{K_{eq,S}}\right] \qquad (4)$$

where $\dot{r}_{MSRR}$ and $\dot{r}_{WGSR}$ are the rate of reactions MSRR and WGSR, respectively. k_{WGSR} and $k_0 = 4274\ mol/(m^2.s.bar)$ are the pre-exponential factors [25], $E_a = 82\ Kj/mol$ is the activation energy [25], and $K_{eq,S}$ is the equilibrium constant for WGSR which is expressed by Eq. (5):

$$K_{eq,S} = \exp\left(-\frac{\Delta G^0}{RT}\right) \qquad (5)$$

Electrons have been observed to transfer between species within the TPB of both electrodes. The area under consideration is distinguished by the convergence of ionic conductors and electron-conducting materials, in addition to the presence of pores within which gas constituents are found [5]. Assuming that methane is consumed exclusively in the MSRR, anodic and cathodic electrochemical processes can be described as Eqs. (6, 7 and 8):

$$H_2 + O^{2-} \rightarrow H_2O + 2e^- \qquad (6)$$

$$CO + O^{2-} \rightarrow CO_2 + 2e^- \qquad (7)$$

$$\frac{1}{2}O_2 + 2e^- \rightarrow O^{2-} \qquad (8)$$

The overall cell reactions can be expressed as follows:

$$H_2 + \frac{1}{2}O_2 \rightarrow H_2O \qquad (9)$$

$$CO + \frac{1}{2}O_2 \rightarrow CO_2 \qquad (10)$$

These two electrochemical reactions are exothermic and serve as sources of heat generation in an SOFC. It is important to acknowledge that the rate of reactions involving H_2 and CO oxidation, as well as O_2 reduction, can be delineated through the application of Faraday's law. This law establishes a correlation between the flow rate of reactants and products and the electric current [5]:

$$\dot{r}_{elec,H_2} = \dot{r}_{elec,H_2O} = \frac{J_{H_2}}{2F} \quad (11)$$

$$\dot{r}_{elc,CO} = \dot{r}_{elec,CO_2} = \frac{J_{CO}}{2F} \quad (12)$$

$$\dot{r}_{elec,O_2} = \frac{J_{O_2}}{4F} \quad (13)$$

where $F = 96485\ C/mol$ stands for the Faraday constant. $\dot{r}_{elec,i}$ defines the rate at which a species is produced or consumed electrochemically. j_{co} and j_{H_2} determine the local current densities produced by CO and H_2 electrochemical reactions. The reversible cell voltage, otherwise known as the open-circuit potential (OCP), is a local parameter that is contingent upon the local temperature and gas composition at the anode and cathode [28]. The determination is made by calculating the difference between the thermodynamic potentials of the electrode reactions, as outlined in the Nernst equation [29]:

$$E^{rev}_{H_2-O_2} = E^{0}_{H_2-O_2} - \frac{RT}{2F}\ln\left[\frac{P^{fc}_{H_2O}}{P^{fc}_{H_2}.\left(\frac{P^{ac}_{O_2}}{100000}\right)^{0.5}}\right] \quad (14)$$

$$E^{rev}_{CO-O_2} = E^{0}_{CO-O_2} - \frac{RT}{2F}\ln\left[\frac{P^{fc}_{CO_2}}{P^{fc}_{CO}.\left(\frac{P^{ac}_{O_2}}{100000}\right)^{0.5}}\right] \quad (15)$$

In these correlations, E^0 is defined as the open-circuit potential at standard temperature and pressure, with unity activity. It can be calculated using the Gibbs free energy change for electrochemical reactions (Eqs. (9 and 10)) [29]:

$$E^{0}_{H_2-O_2} = -\frac{\Delta G^0}{2F} = -\frac{g^0_{H_2O} - {}^1/_2\, g^0_{O_2} - g^0_{H_2}}{2F} \quad (16)$$

$$E^{0}_{CO-O_2} = -\frac{\Delta G^0}{2F} = -\frac{g^0_{CO_2} - {}^1/_2\, g^0_{O_2} - g^0_{CO}}{2F} \quad (17)$$

In the event of electrical current being derived from a fuel cell, a decrease in voltage is observed in response to five distinct cell loss mechanisms. The mechanisms in question are electrode activation and concentration overpotentials and internal resistances. In the SOFC, the reactive gas species must find a path from the flow ducts through a porous material to the anodic and cathodic TPB, respectively. Conversely, the H_2O and CO_2 produced must traverse from the anode side TPB to the fuel duct through the porous media. Due to the diffusive nature of the porosity of the electrode, the mole fraction of the reacting species at the TPB differs from the bulk concentration. The Nernst formula, when written using the reactant concentration on the TPBs, indicates that the resulting no-load voltage would be lower than that obtained from formulae (14) and (15). Dalton's law is a fundamental principle in electrochemistry that enables the calculation of concentration overpotentials for both anode and cathode electrodes [29]:

$$\eta_{conc,H_2} = -\frac{RT}{2F}\ln\left[\frac{X^{TPB}_{H_2}.X^{fc}_{H_2O}}{X^{fc}_{H_2}.X^{TPB}_{H_2O}}\right] \quad (18)$$

$$\eta_{conc,CO} = -\frac{RT}{2F}\ln\left[\frac{X^{TPB}_{CO}.X^{fc}_{CO_2}}{X^{fc}_{CO}.X^{TPB}_{CO_2}}\right] \quad (19)$$

$$\eta_{conc,O_2} = -\frac{RT}{4F}\ln\left[\frac{X^{TPB}_{O_2}}{X^{ac}_{O_2}}\right] \quad (20)$$

X_i are species mole fractions, $i \in \{H_2, H_2O, CO, CO_2, O_2, CH_4\}$. The parameters *fc* and *ac* refer to the fuel and air ducts, respectively. The mole fraction of reactant species at the anode and cathode TPB can be evaluated by following equations [29]:

$$X^{TPB}_{H_2} = X^{fc}_{H_2} - \frac{j_{H_2}RT_{PEN}t_{an.}}{2FP^{fc}D_{eff,H_2}} \quad (21)$$

$$X^{TPB}_{H_2O} = X^{fc}_{H_2O} + \frac{j_{H_2}RT_{PEN}t_{an.}}{2FP^{fc}D_{eff,H_2O}} \quad (22)$$

$$X^{TPB}_{CO} = X^{fc}_{CO} - \frac{j_{CO}RT_{PEN}t_{an.}}{2FP^{fc}D_{eff,CO}} \quad (23)$$

$$X^{TPB}_{CO_2} = X^{fc}_{CO_2} + \frac{j_{CO}RT_{PEN}t_{an.}}{2FP^{fc}D_{eff,CO_2}} \quad (24)$$

$$X^{TPB}_{O_2} = 1 + \left(X^{ac}_{O_2} - 1\right).\exp\left(\frac{J_{O_2}RT_{PEN}t_{ct.}}{4FP^{ac}D_{eff,O_2}}\right) \quad (25)$$

The effective diffusion coefficient will be expressed as described in refs. [25, 35, 37, 38]. The activation overpotentials that are attributable to the energy barriers necessary to initiate a reaction are expressed by the non-linear Butler-Volmer equation for cathode and anode electrodes [36, 38-40]:

$$j_{O_2} = j_{0,O_2}\cdot\left[\exp\left(\frac{F\eta_{act,O_2}}{RT}\right) - \exp\left(-\frac{F\eta_{act,O_2}}{RT}\right)\right] \quad (26)$$

$$j_{H_2} = j_{0,H_2}\cdot\left[\exp\left(\frac{2F\eta_{act,H_2}}{RT}\right) - \exp\left(-\frac{F\eta_{act,H_2}}{RT}\right)\right] \quad (27)$$

$$j_{CO} = j_{0,CO}\cdot\left[\exp\left(\frac{2F\eta_{act,CO}}{RT}\right) - \exp\left(-\frac{F\eta_{act,CO}}{RT}\right)\right] \quad (28)$$

where $j_{0,i}$ define the exchange current densities and have been calculated as follows [25]:

$$j_{0,H_2} = (2.1\times10^{11}) \frac{RT}{F}\cdot\left(\frac{X_{H_2O}}{X_{H_2}.K_{eq,H_2}}\right)^{0.266}\exp\left(-\frac{120000}{RT}\right) \quad (29)$$

$$j_{0,CO} = (0.84\times10^{11}) \frac{RT}{F}\cdot\left(\frac{X_{CO_2}}{X_{CO}.K_{eq,CO}}\right)^{0.266}\exp\left(-\frac{120000}{RT}\right) \quad (30)$$

$$j_{0,O_2} = (1.175\times10^{11})\frac{RT}{F}\exp\left(-\frac{137000}{RT}\right) \quad (31)$$

The ohmic losses are the same as those described in Ref. [37]. To account for the two electrochemical reactions of H_2 and CO, the parallel circuit model shown in Fig. 2 is employed [29]. The local single-cell potential is obtained by the following two relations:

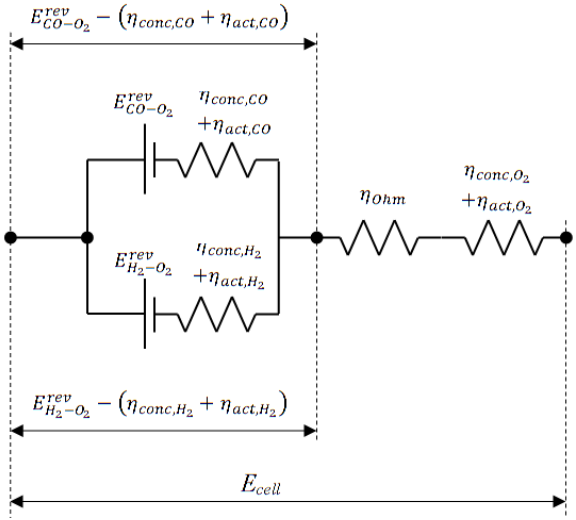

Fig. 2. Equivalent circuit model for current and voltage calculations.

$$E_{cell} = E^{rev}_{H_2-O_2} - (\eta_{conc,O_2} + \eta_{act,O_2}) - (\eta_{conc,H_2} + \eta_{act,H_2}) - \eta_{Ohm} \quad (32)$$

$$E_{cell} = E^{rev}_{CO-O_2} - (\eta_{conc,O_2} + \eta_{act,O_2}) - (\eta_{conc,CO} + \eta_{act,CO}) - \eta_{Ohm} \quad (33)$$

Finally, the local current density of the cell can be determined by:

$$j_{cel} = j_{O_2} = j_{H_2} + j_{CO} \quad (34)$$

J_{cel} is the cell local current density. According to the iterative procedure proposed by Iwai *et al.* [29], the ratio of J_{H2} and J_{CO} is determined so that the potentials obtained for the parallel part of Fig. 2 match each other.

2.2.2. *Species mass balances*

The mass conservation of the species, taking into account the one-dimensional control volume and Fick's law, regarding steady plug flow and constant axial velocity for the flow can be expressed as follows [25, 40]:

$$u_x\frac{d\rho_A}{dx} = \dot{m}'''_A \quad (35)$$

where $\dot{m}'''_A$ defines the net species production rate by chemical or electrochemical reaction per unit volume. Therefore, in both the anode and cathode channels, the following correlations can guarantee the preservation of the mass of the gaseous species of interest [25, 40]:

$$\frac{d\rho_{O_2}}{dx} = -\frac{1}{u_a}.\frac{A_{re}.M_{O_2}.\dot{r}_{elec,O_2}}{V_{ac}} \quad (36)$$

$$\frac{d\rho_{N_2}}{dx} = 0 \quad (37)$$

$$\frac{d\rho_{CH_4}}{dx} = -\frac{1}{u_f}.\frac{A_{re}.M_{CH_4}.\dot{r}_{MSRR}}{V_{fc}} \quad (38)$$

$$\frac{d\rho_{H_2}}{dx} = \frac{1}{u_f}.\frac{A_{re}.M_{H_2}.(3\dot{r}_{MSRR} + \dot{r}_{WGSR} - \dot{r}_{elec,H_2})}{V_{fc}} \quad (39)$$

$$\frac{d\rho_{CO}}{dx} = \frac{1}{u_f}.\frac{A_{re}.M_{CO}.(\dot{r}_{MSRR} - \dot{r}_{WGSR} - \dot{r}_{elec,CO})}{V_{fc}} \quad (40)$$

$$\frac{d\rho_{CO_2}}{dx} = \frac{1}{u_f}.\frac{A_{re}.M_{CO_2}.(\dot{r}_{WGSR} + \dot{r}_{elec,CO})}{V_{fc}} \quad (41)$$

$$\frac{d\rho_{H_2O}}{dx} = \frac{1}{u_f}.\frac{A_{re}.M_{H_2O}.(-\dot{r}_{MSRR} - \dot{r}_{WGSR} + \dot{r}_{elec,H_2})}{V_{fc}} \quad (42)$$

where A_{re} is the reaction area, and M_i stands for the molecular mass of components $i \in \{H_2, H_2O, CO, CO_2, O_2, CH_4, N_2\}$.

2.2.3. *Energy balances*

A separate analysis has been conducted to ascertain the governing energy balance for the PEN, interconnect, air, and fuel channels. For the solid structures (PEN and interconnect), the predominant heat transfer mechanisms are convection between the solid structures and the gas flows, as well as the conductive heat flux. In the gas channels, the convection mechanism in the longitudinal axes of the channels has also been taken into consideration. Furthermore, radiation between the PEN and interconnect, attributable to the elevated operating temperature of the cell, has been duly considered. The enthalpies of MSRR and WGSR are delivered in the fuel duct, and the enthalpies of electrochemical reactions and electrical resistance in the PEN structure serve as heat sources. Consequently, the subsequent equations have been deduced for the conservation of energy in distinct structures [24, 25, 34]:

Air channel:

$$\rho_a u_a C_{p,a} V_{ac} \frac{dT_{ac}}{dx} = h_{c,PEN-a} A_{PEN,S}(T_{PEN} - T_{ac}) + h_{c,int-a} A_{int,S}(T_{int} - T_{ac}) \quad (43)$$

Fuel Channel:

$$\rho_f u_f C_{p,f} V_{fc} \frac{dT_{fc}}{dx} = h_{c,PEN-f} A_{PEN,S}(T_{PEN} - T_{fc}) + h_{c,int-f} A_{int,S}(T_{int} - T_{fc}) - A_{re}(\dot{r}_{MSRR}.\Delta H_{MSRR} + \dot{r}_{WGSR}.\Delta H_{WGSR}) \quad (44)$$

PEN structure:

$$0 = V_{PEN} K_{PEN} \frac{d^2 T_{PEN}}{dx^2} - h_{c,PEN-f} A_{PEN,S}(T_{PEN} - T_{fc}) - h_{c,PEN-a} A_{PEN,S}(T_{PEN} - T_{ac}) - A_{re}(\dot{r}_{elec,H_2}.\Delta H_{elec,H_2} + \dot{r}_{elec,CO}.\Delta H_{elec,CO}) - j_{cell} E_{cell} A_{re} - \dot{E}_{rad}''.A_{re} \quad (45)$$

Interconnect:

$$0 = V_{int} K_{int} \frac{d^2 T_{int}}{dx^2} - h_{c,int-f} A_{int,S}(T_{int} - T_{fc}) - h_{c,int-a} A_{int,S}(T_{int} - T_{ac}) + \dot{E}_{rad}''.A_{re} \quad (46)$$

2.2.4. *Performance factors*

Two primary factors must be considered when determining the amount of fuel and air necessary to generate a specific amount of electricity. The aforementioned factors include the fuel utilization factor and the air ratio, which can be defined using the following equations [24, 25, 34]:

$$U_f = \frac{j_{avg} LW}{(8FX^0_{CH_4} + 2FX^0_{H_2} + 2FX^0_{CO})\dot{N}^0_{fuel}} \quad (47)$$

$$U_a = \frac{j_{avg} LW}{(4FX^0_{O_2})\dot{N}^0_{air}} \quad (48)$$

J_{avg} is the average current density of the cell. Fuel and air utilization factors are the proportions of fuel and air used by the cell to produce electricity. The air ratio represents the excess air relative to the stoichiometrically required air for cooling purposes [25] and is mathematically the inverse of the air utilization factor:

$$\lambda_a = \frac{1}{U_a} \quad (49)$$

The electric power and fuel efficiency are defined as follows [24, 25, 34]:

$$P_{SOFC} = j_{avg} E_{cel} \quad (50)$$

$$\varepsilon_{SOFC} = \frac{j_{avg} E_{cell} LW}{\left(X^0_{CH_4} LHV^0_{CH_4} + X^0_{H_2} LHV^0_{H_2} + X^0_{CO} LHV^0_{CO}\right) \dot{N}^0_{fuel}} \quad (51)$$

The term 'fuel efficiency' is understood to denote the proportion of the total electrochemical energy of the fuel at the inlet that is capable of being converted into electricity.

2.3. *Procedure for simulation and model validation*

The simulation is executed using a program code that has been internally developed and is written in Compaq Visual Fortran 90. The species mass conservation and energy conservation equations are discretized by the finite difference method and then solved iteratively. As demonstrated in the literature, there are two approaches to distributed modeling of SOFCs: providing the operating voltage and providing the cell average current density. In this study, the second approach is employed, and the corresponding algorithm is shown in Fig. 3. In both approaches, the fuel cell is considered as a set of parallel discrete elements with uniform operating voltage and non-uniform local current densities. Consequently, two algebraic loops have been implemented for the iterative solution of the governing equations: one loop for the iteration of the cell voltage and the other for the iterative solution of the conservation of species mass and energy equations with given local current density and cell voltage. The computational area is segmented into four layers: the PEN structure, the fuel flow channel, the air flow channel, and the interconnector. The discretization of each layer is conducted along the flow direction, with the distance between every two grid points in all layers being set at 4 millimeters. It is observed that the results are less dependent on the grid size. For the purpose of accelerating the rate of convergence of the computation, this value is selected.

The present model is predicated on certain assumptions, including the use of syngas as fuel, disparate inlet and outlet temperatures, and the electrochemical reaction of both H_2 and CO. These assumptions render it difficult to locate experimental data from the literature that would allow for the validation of the model. Consequently, the remaining numerical reports are utilized for the purpose of comparison and the certification of results.

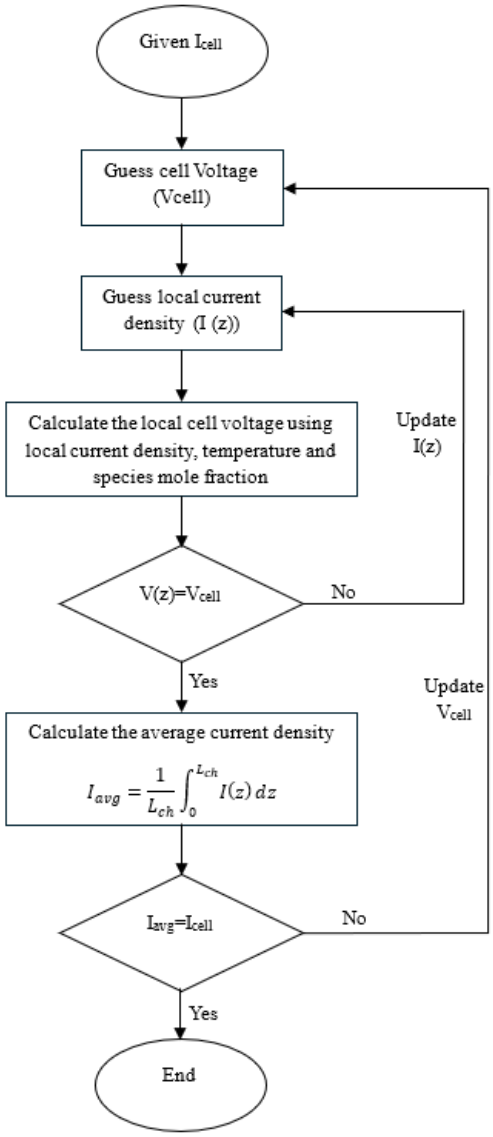

Fig. 3. Algorithm to calculate the cell voltage and local current density.

The model developed in the present study is founded on models proposed by Aguiar *et al.* [25] and Iwai *et al.* [29]. In the initial phase, the validity of the model was confirmed by Aguiar *et al.* [25], who exclusively considered H_2 electrochemical oxidation. The ensuing section will present a comparison of the corresponding results, including the distribution of the species concentration, the temperature in all four layers, the local current density, and other electrical performance factors along the cell length in two

models. In the second step of the model validation process, both H_2 and CO were implicated in the electrochemical reaction. The outcomes were then compared to those reported in the study by Iwai *et al.* [29].

3. Simulation results and discussion

3.1. Input data and computational condition

The fuel cell characteristics follow those of Aguiar *et al.* [25] as summarized in Table 1.

Table 1. Cell dimension and material properties.

Cell dimension:	
Cell length	0.4 m
Cell width	0.1 m
Height of fuel channel	0.001m
Height of air channel	0.001m
Anode thickness	500 µm
Cathode thickness	50 µm
Electrolyte thickness	20 µm
Interconnect thickness	500 µm
Material properties:	
PEN thermal conductivity	2×10^{-3} kw/mK
Interconnect thermal conductivity	25×10^{-3} kw/mK
PEN emissivity	0.8
Interconnect emissivity	0.1
Electrodes porosity	0.3
Electrode tortuosity	6
Average pore radius	0.5 µm
Electrodes porosity	0.3

The mole flow rates of gas streams can be calculated using Eqs. (47 and 49) by means of a given air ratio, fuel utilization factor, and average cell current density. The composition of the fuel supplied is determined from a gas mixture with a steam to carbon ratio of 2 and a pre-reforming rate of 10% methane. The mole fractions of the gas species in such a mixture are given in Table 2.

It has been established that the inlet temperature of the gas flows is precisely 1023 K, while the pressure is 1 bar. The thermal conductivity of the solid components is assumed to be constant, unlike Aguiar *et al.* [25], the temperature-dependent thermal conductivity of the gas mixtures in both air and fuel channels is calculated locally [41], and the Nusselt number is determined to be 2.97 [32]. The effective diffusion coefficients of the porous materials, unlike the compared reference, are evaluated as explained in ref. [37]. The assumption of the temperature dependence of the resistivity of the electrodes and the electrolyte is the other detail taken into account in this study [37]. All results are obtained under the following conditions: a fuel utilization factor of 0.75, an air ratio of 8.5, and a cell average current density of 5000 A/m^2. The remaining gas mixture properties (gas flow densities and heat capacities), the temperature-dependent reaction enthalpies, and Gibbs free energies are determined by virtue of the Ideal Gas Assumption. In addition to the inlet temperature and pressure, a uniform axial velocity at the channel inlet is assumed. Adiabatic conditions are also applied at both ends of the PEN and interconnect structures.

3.2. Results considering H_2 electrochemical reaction

This section focuses on the validation of the model developed in the current study and also the generation of basic results for the given operating conditions, as outlined in Section 3.1.

Table 2. Inlet fuel composition with 10% pre-reforming.

Description	Mole fractions
CH_4	0.2812
H_2	0.1206
CO	0.0043
CO_2	0.0269
H_2O	0.5668

The subsequent section will address the impact of the CO electrochemical oxidation on these fundamental outcomes. The characteristic curves for power density, cell voltage, and polarization versus current density of the cell are depicted in Fig. 4 and 5, respectively. It is important to acknowledge that the curves depicted in Figs. 4 and Fig. 5 are derived exclusively through the application of the electrochemical model. The pre-reforming rate is equivalent to 1, which stipulates a state of completely steam-reformed methane. The operating temperature and pressure are measured at 1073 kelvin and one bar, respectively.

As demonstrated in Fig. 4, the power density attains its maximum value when the current density is equivalent to 20000 A/m^2. The corresponding voltage and power density are equal to 0.4156 V and 8313.04 W/m^2, respectively. A comparison with Aguiar *et al.* [25] is presented in Table 3. As illustrated in Fig.

4 and Table 3, there is a high degree of congruence with the reference. At the point of maximum power density, as illustrated in Fig. 5, the PEN ohmic loss and the activation polarizations of the cathode and anode are the main sources of loss of the cell's open circuit potential. Conversely, the concentration losses are relatively small. As illustrated in Fig. 5, the cathode concentration polarization is considerably less pronounced in comparison to that of the anode. This phenomenon can be attributed to the comparatively greater thickness of the anode relative to the cathode. The convex curvature of the concentration polarization at low current density, as previously noted in the literature [25, 40], is evident in Fig. 5. The concentration overpotential demonstrates a concave curvature at elevated current density [40]. The curvature of the cell voltage-current density curve is associated with the curvature of the concentration and activation polarizations at low or high current density. However, as demonstrated in [25, 40], the observation of concave curvature at high current density is contingent upon the comparative values of ohmic and activation losses. For the selected parameters and operating conditions, the cell voltage undergoes a decline to zero when the current density attains a value of 43812.5 A/m^2. Consequently, no concave curvature is observed. Indeed, the occurrence of this phenomenon can be attributed to high ohmic and activation losses at high current density. The current density at which the cell operating voltage is reduced to zero is denoted as the limiting current density. Conversely, the activation polarization of the cathode exhibits a higher value in comparison to that of the anode across the entire range of current densities. This phenomenon can be attributed to the comparatively lower exchange current density of the cathode [40].

Table 3. Comparison of cell peak power density and corresponding cell voltage and current density.

Description	Current model	Aguiar [25]	Difference (%)
Power (W/m^2)	8313.04	8600	3.34
Voltage (V)	0.416	0.415	0.24
Current density (A/m^2)	20400	20700	1.45

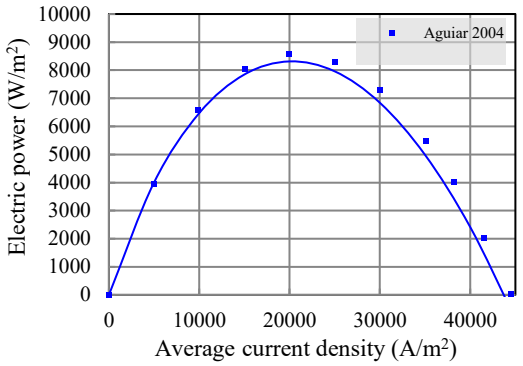

Fig. 4. The variation of cell power density in relation to current density for given operating condition.

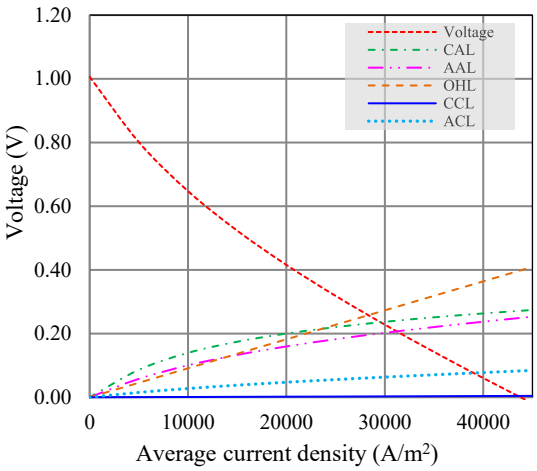

Fig. 5. The variation of cell voltage and polarization curves in relation to current density for given operating condition (current model).

Given the cell's normal operating voltage of 0.6-0.7 V, the best operating range for current density is between 8287.85 and 11905.72 A/m^2, resulting in power densities between 5628.46 and 6997.29 W/m^2. As illustrated in Fig. 6, the predicted cell open circuit potential (OCP) and the effect of polarizations on the OCP are demonstrated. The calculation of the cell's operating voltage is contingent upon the consideration of these parameters.

Comparison with Aguiar *et al.* [25] is also presented. A small deviation between the current model and Aguiar *et al.* [25] is caused by some details considered in the current model, as mentioned in Section 3.1.

The findings of the concurrent resolution of the aforementioned governing equations for four layers are depicted in Fig. 7 to Fig. 11 for the operating conditions given in Table 1 and Table

2.The mole fraction curves of the gas species in the fuel flow duct are illustrated in Fig. 7. The concurrent occurrence of MSRR, WGSR, and electrochemical reaction establishes the sink and/or source terms for the alterations in species mole fractions. Additionally, the local temperature exerts an indirect influence on the local composition of the gas mixture through the temperature-dependent reaction rates. Conversely, the electric performance of the cell, that is to say, the cell current density and voltage, exerts a comparable effect.

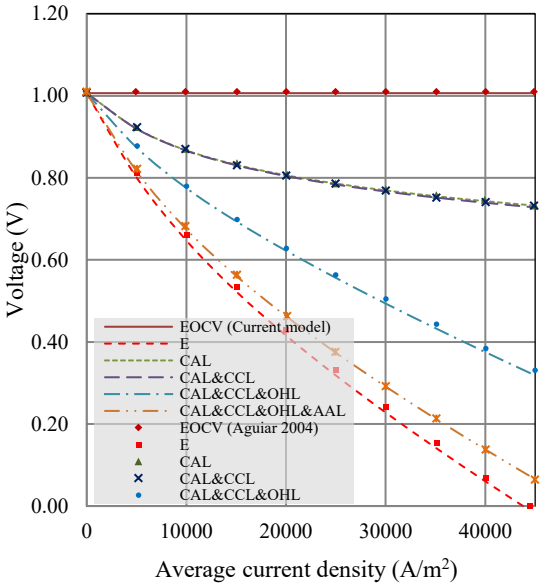

Fig. 6. The effect of various polarizations on cell voltage as a function of cell current density.

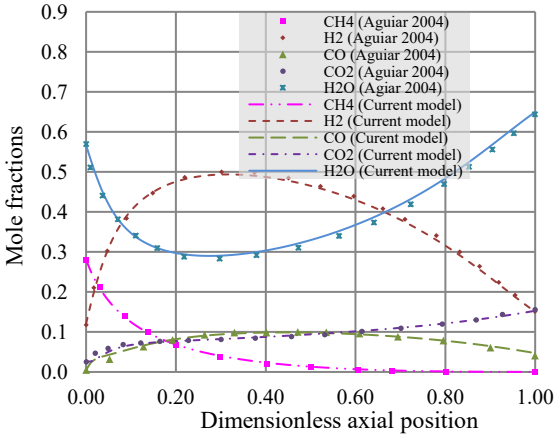

Fig. 7. The longitudinal molar fraction variation of gas species in the fuel flow duct.

Consequently, both the local temperature and the electrical performance of the cell are strongly influenced by the composition of the gas mixture. Upon entry of the fuel into the duct, the MSRR is initiated with a high reaction rate, attributable to the elevated methane content.

The decline in methane concentration, as illustrated in Fig. 7, substantiates the accelerated reaction rate of the MSRR. The primary and most significant consequence of this elevated reaction rate is the swift consumption of heat by the highly endothermic MSRR. On the other hand, the low hydrogen content of the fuel is responsible for the low local current density at the inlet of the fuel duct, and consequently for the low heat production in this region. This assertion is corroborated by the findings depicted in Fig. 7. The process of methane consumption results in the generation of hydrogen and carbon monoxide, concurrently leading to water consumption. It has been demonstrated that the vast majority of methane is consumed until $\frac{x}{L_c} = 0.7$, at which point hydrogen reaches its peak value at $\frac{x}{L_c} = 0.31$. At this juncture, the electrochemical oxidation reaction rate becomes a more rapid process. Concurrently, hydrogen consumption and water production are accelerated. The decreasing trend of the hydrogen mole fraction and increasing behavior of the water mole fraction along the cell length after this point can be clearly seen in Fig. 7. The local current density profile illustrated in Fig. 8 supports this treatment of the hydrogen electrochemical oxidation reaction rate. From the other viewpoint, an augmented electrochemical reaction rate will invariably result in the release of a substantial quantity of heat, thereby precipitating an escalation in the local temperature of the four layers.

As the temperature increases, the activation polarization and ohmic losses decrease, as illustrated in Fig. 9. As demonstrated in Fig. 7, there is a minor discrepancy between the findings of the current model and those of Aguiar *et al.* [25]. This deviation is attributed to the disparate local current densities observed in both models, as shown in Fig. 8, and the divergent temperature distributions along the cell length, as depicted in Fig. 10 and Fig. 11. Notwithstanding this minor incongruity, it can be concluded that the current model has accurately predicted the distribution of gas constituent mole fractions along the cell.

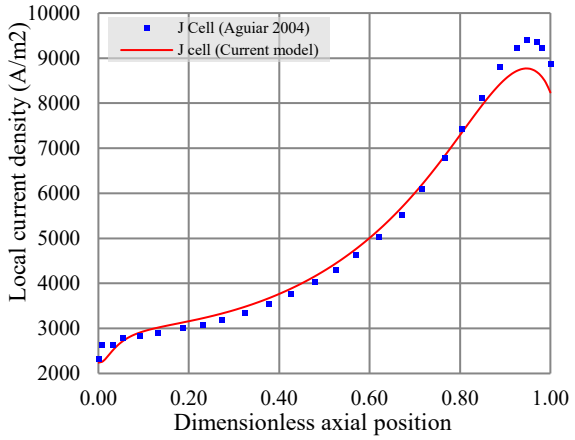

Fig. 8. The longitudinal variation of local current density.

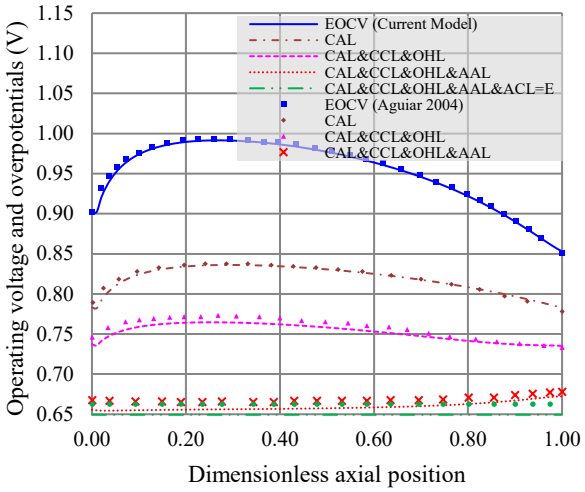

Fig. 9. The longitudinal variation of cell operating voltage and distribution of overpotentials.

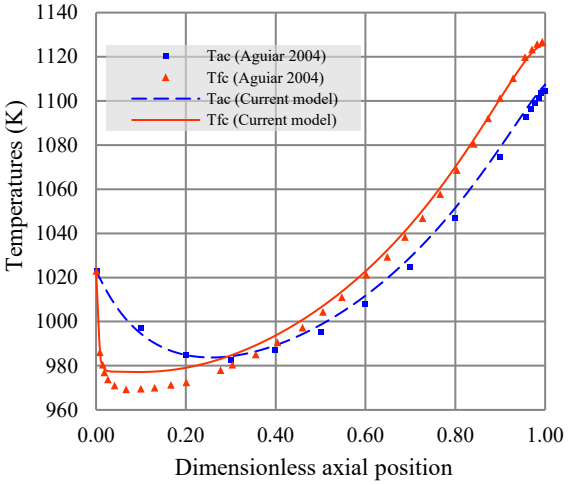

Fig. 10. The longitudinal variation of air and fuel channel temperature.

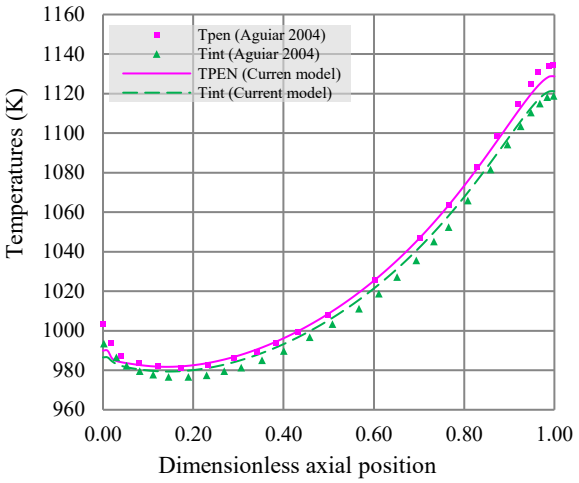

Fig. 11. The longitudinal variation of interconnect and PEN structure temperature.

As demonstrated in the preceding discussion, the non-uniform heat generation within the cell constitutes the primary factor contributing to the substantial temperature gradient that is observed along the cell length. As shown by Aguiar *et al.*[25], a minor decline in the temperature of fourfold layers has been observed to be concomitant with the process of methane reforming. However, as the MSRR rate decreases and the hydrogen electrochemical reaction becomes predominant, the rate of heat generation becomes dominant. Consequently, an increase in temperature along the cell length can be observed. Although the calculated longitudinal variation of temperature of flow ducts, the PEN structure, and the interconnect, as determined by the current model, are marginally higher than those reported by Aguiar *et al.*[25]. The observed deviation is attributed to the presence of different Nusselt numbers, temperature-dependent thermal conductivity of the gas mixture, and different diffusion mechanisms. These elements contributed to the different electrical performance of the cell.

The predicted cell current density, cell voltage, and the effect of different polarizations are shown in Fig. 8 and 9, respectively. According to Eq. (14), it can be deduced that the cell open circuit potential (OCP) exhibits an increase in response to a decrease in water partial pressure, concurrent with an increase in hydrogen partial pressure. This phenomenon is exemplified in Fig. 9. Thereafter, a decreasing trend in the cell

OCP is predicted in response to variation in the composition of the gas mixture and temperature. A decrease in local temperature is accompanied by an augmentation in the ionic resistivity of the electrolyte and the activation overpotential [29]. This treatment is indicated in Fig. 9. The ohmic loss and the activation loss increase up to $\frac{x}{L_c} = 0.23$, where the temperature of the PEN structure is around its minimum value. However, these terms of overpotentials serve to curtail the local temperature increases, thereby enabling the current density to increase. It is important to note that the concentration polarization increases along the cell length. This increase is a result of the consumption of the reactant.

As demonstrated in Fig. 10 and 11, the maximum discrepancy between the two models is observed to be; 0.89% for the air channel, 1.5% for the fuel channel, 0.81% for the PEN structure, and 1.12% for the interconnect. The most significant temperature gradient is observed in the PEN structure, with a magnitude of 150.1 K, spanning from a minimum of 987.71 K to a maximum of 1137.81 K at the outlet of the cell.

Finally, it should be mentioned that the cell operating voltage, power density, and fuel efficiency of the case studied here are equal to 0.65 V, 3247 W/m^2, and 45.83 %, respectively. The corresponding values obtained by Aguiar *et al.*[25] are 0.66 V, 3320 W/m^2, and 46.8%, respectively. The current model's performance characteristics have been shown to be in alignment with those of the compared reference, thereby validating the model's capacity for predicting SOFC performance. This finding paves the way for further investigation into the impact of various parameters, including the electrochemical oxidation of carbon monoxide.

3.3. Effects of co electrochemical oxidation

As mentioned in the previous section, only H_2 was involved in the electrochemical reaction. However, in this section, both CO and H_2 are considered in the electrochemical reaction on the anode side. Prior to the investigation of the effect of the electrochemical reaction of the CO on the electric performance of the SOFC, the model was validated based on some available literature, such as Iwai *et al.*[29]. The simulations were performed with the data provided in the Iwai *et al.*[29], and the resulting comparison is presented in Table 4. The maximum temperature was detected at the cell outlet, and the deviation between the two numerical methods was found to be approximately 9%. This difference can be attributed to the differing approaches of the models and also the varying heat transfer mechanisms considered in the conservation of energy equation. Iwai *et al.*[29] did not take radiative heat transfer into consideration. The interconnection between the temperature field and the electrochemical model is of particular concern, as any deviation in the temperature distribution can have a direct impact on the electric performance. However, as demonstrated by Andersson *et al.*[5], CO accounts for 15-20% of the total current density. At the point of maximum local current density, this fraction for CO reaches 17%, showing a reliable value.

The remainder of this section discusses the effects of considering the CO as a fuel on the cell performance and operating parameters. To this end, the whole model described in Section 2.2 is solved numerically with the data given in Table 1.

Table 4. Comparison of cell performance in current model with those of Iwai *et al.*[29], J_{avg}= 3000 A/m^2 and pre-reforming rate is 0.3.

Description	Current model	Iwai [29]	Difference (%)
Power (W/m^2)	2310	2234	3.4
Voltage (V)	0.768	0.745	3.1
$T_{PEN,\,max}$ (k)	1058.23	1167.27	9.3
J_{H2}/J_{Total}	0.83	0.72	15.3
J_{CO}/J_{Total}	0.17	0.28	39.3

On the other hand, the results of Section 3.2 are compared in this section with the incorporation of CO on the anode side electrochemical reactions. It is important to note that the average current density and the pre-reforming rate in this section are set equal to 5000 A/m^2 and 0.3, respectively.

Fig. 12 shows the mole fraction of the gas species of the fuel channel with and without considering CO as a reactant at the anode side TPB. The trends of the profiles and the corresponding interpretations are analogous to the previous section, with the focus here being on the comparison of two cases; Case 1 refers to the H_2 electrochemical oxidation only, and Case 2 refers to the condition where both CO and H_2 react at the anode side TPB reactions. The profile

of the methane mole fraction along the cell is nearly identical in both cases, indicating that the presence of CO in the anode electrochemical reaction does not affect the consumption rate of the methane. However, as demonstrated in Fig. 12, the deviation of the hydrogen and water mole fractions gradually becomes apparent. The decrease in the amount of CO involved in the WGSR is the primary effect of the CO electrochemical reaction. Consequently, the rates at which H_2 is produced and subsequently H_2O is consumed by the WGSR are lower than in Case 1. On the other hand, the production rate of CO_2 is accelerated by the electrochemical reaction of CO.

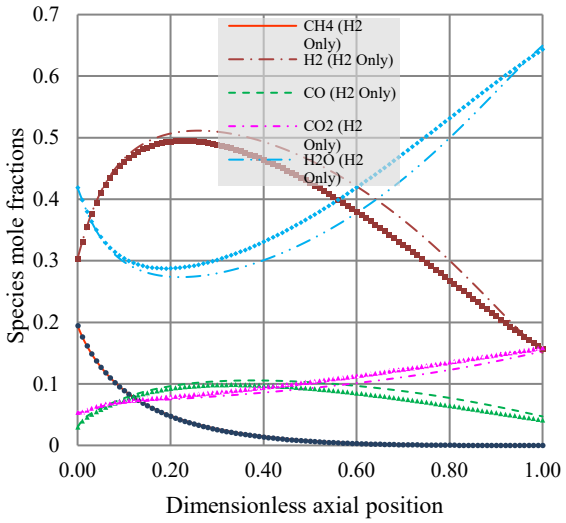

Fig. 12. The longitudinal variation of species concentration affected by the CO electrochemical reaction.

Finally, all the above-mentioned effects lead to a decrease in the mole fractions of H_2 and CO, and an increase in the mole fractions of H_2O and CO_2 in Case 2, as depicted in Fig. 12. The temperature profiles along the cell length for the air and fuel channels are presented in Fig. 13, while Fig. 14 shows the similar profiles for the interconnect and the PEN structure. As previously discussed, the cell contains three distinct heat sources: WGSR, the H_2 and CO electrochemical reactions. Additionally, the methane steam reforming reaction functions as a heat sink within the cell. The interaction between these terms can result in either cooling or heating effects within the SOFC. Fig. 12 shows that the rate of methane consumption remains constant when CO is present in the electrochemical reaction.

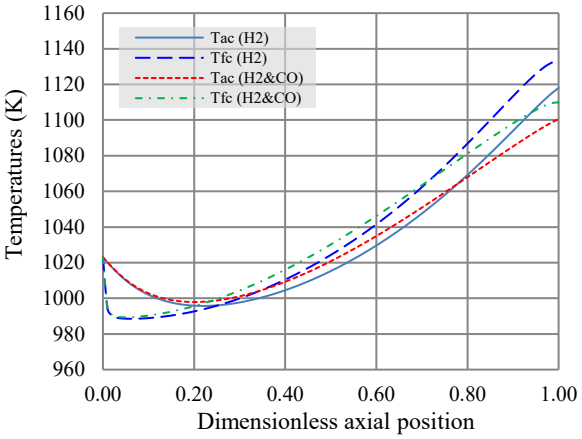

Fig. 13. The Longitudinal variation of fuel temperature affected by CO electrochemical reaction.

.

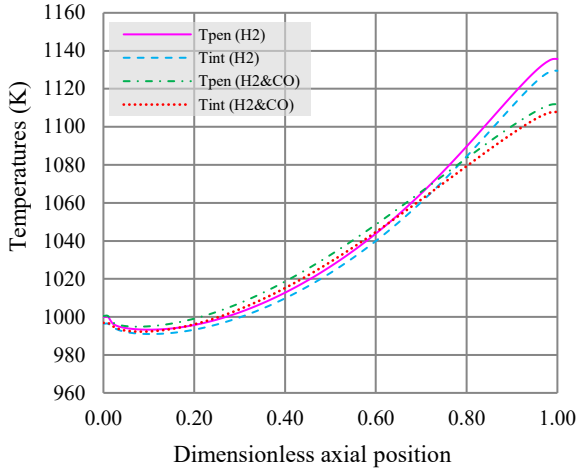

Fig. 14. The longitudinal variation of PEN and interconnect affected by the CO electrochemical reaction.

This indicates that the rate of heat consumption remains unchanged in both scenarios. However, the concentration of H_2 in Case 2 is lower than in Case 1, which leads to a decrease in the heat generation by the H_2 electrochemical reaction. On the other hand, the presence of CO in the electrochemical reaction results in increased heat generation compared to scenarios where CO only participates in the WGSR. In summary, it can be concluded that the inclusion of CO in the anode-side electrochemical reaction, in addition to H_2, leads to enhanced heat production within the cell. Therefore, the temperature of the four

layers at each point along the cell length for Case 2 is marginally higher than that of Case 1, as illustrated in Fig. 13 and Fig. 14.

As illustrated in Fig. 15 and 16, the electric performance of the cell exhibits variation in terms of current density, voltage, and overpotentials along the cell length. As demonstrated in the preceding section, an elevation in operating temperature results in a reduction of overpotentials, thereby inducing an increase in the corresponding current density. Accordingly, as demonstrated in Fig. 15, the total local current density in Case 2 exceeds that of Case 1. Fig. 17 compares the anode and cathode activation and concentration overpotentials for two cases. The presence of CO in the electrochemical reaction has been demonstrated to reduce both the anode and cathode activation losses, as evidenced by the research conducted by Iwai *et al.*[29] and Andersson *et al.*[5].

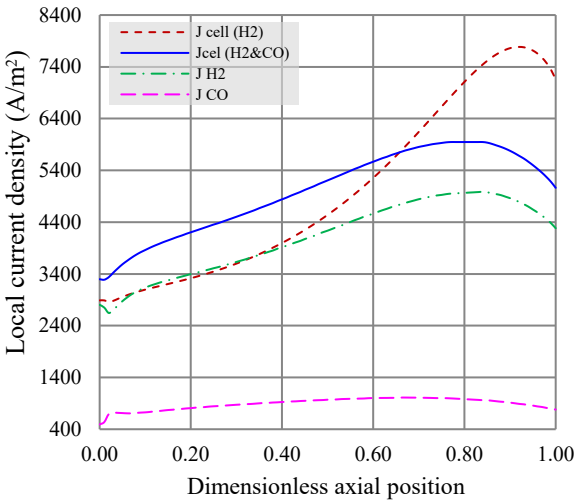

Fig. 15. The longitudinal variation of local current density affected by the CO electrochemical reaction.

At the entrance of the cell, the total local current density is 3291.77 A/m^2, of which approximately 15%, equivalent to 494.2 A/m^2, is produced by CO, and the remainder, 85%, equivalent to 2803.57 A/m^2, is produced by H_2. At the point of maximum local current density, the ratio of CO to H_2 is 16.17% and 83.83%, respectively.

The contribution of CO to the current density is within the acceptable range reported by Andersson *et al.*[5]. Furthermore, Eqs. (14 and 15) indicate that the cell open circuit potential depends on both the temperature and the composition of the gas mixture.

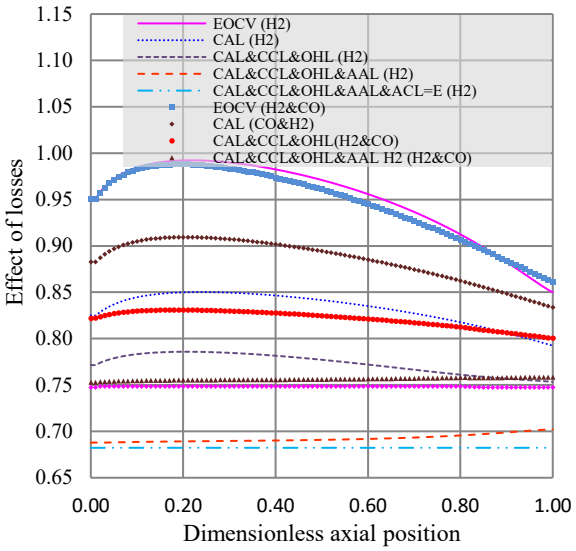

Fig. 16. The longitudinal variation of the cell operating voltage and overpotentials affected by the CO electrochemical reaction.

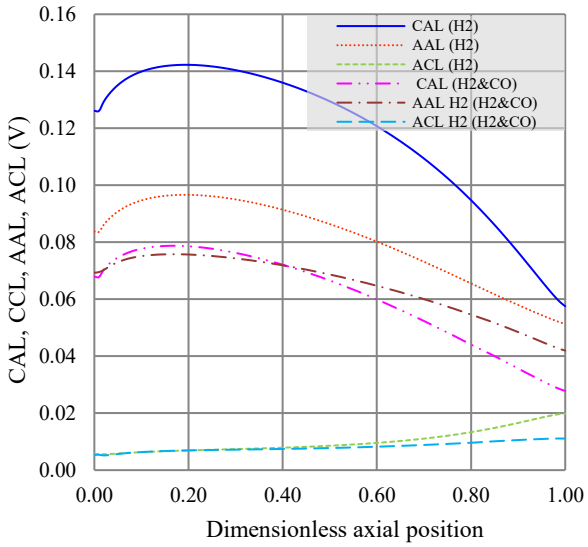

Fig. 17. Comparison of activation and concentration losses with or without CO electrochemical reaction.

At the cell inlet, the composition of the incoming gas (fuel) and the inlet temperature are identical in two cases. Consequently, the OCP of the cell is equivalent in both cases. However, as the study progresses, discrepancies emerge in the temperature field and the mole fractions of the species between the two cases. Consequently, the disparity in the cell OCP becomes evident. Conversely, a decrease in H_2O (or CO_2) and an

increase in H_2 (or CO) will increase in the cell OCP, as demonstrated by Eqs. (14 and 15). It has been demonstrated that, given the lower concentration of H_2O in Case 2 relative to the corresponding value in Case 1 and the higher concentration of H_2 in Case 2, the cell OCP in Case 2 is lower than that in Case 1 after ($\frac{x}{L_c} \cong 0.1$), as illustrated in Fig. 16. Considering the effects of polarization losses, as indicated in Fig. 17 and discussed above, the comparison of the cell operating voltage, power density, and fuel efficiency for both cases is presented in Table 5. It can be concluded that the presence of CO in the electrochemical reactions has the potential to enhance the electric performance of the cell and facilitate the efficient production of electric current. Furthermore, it is anticipated that the overpotentials will decrease, and the operating voltage and power density will increase accordingly.

Finally, a comparison of the open circuit potentials corresponding to the CO and H_2 electrochemical reactions is depicted in Fig. 18, and a comparison of the corresponding activation and concentration polarizations is shown in Fig. 19. It is evident that the calculated OCPs remain constant along the cell. However, the anode activation polarization related to H_2 is greater than that of CO. Furthermore, the concentration polarization of CO, due to its lower concentration, is greater than that of H_2.

Table 5. Comparison of cell performance in two cases; with or without CO electrochemical reaction.

Description	H_2 only	Both CO and H_2
power (W/m^2)	3411.396	3739.130
Voltage (V)	0.68	0.75
Fuel efficiency (%)	0.46	0.50

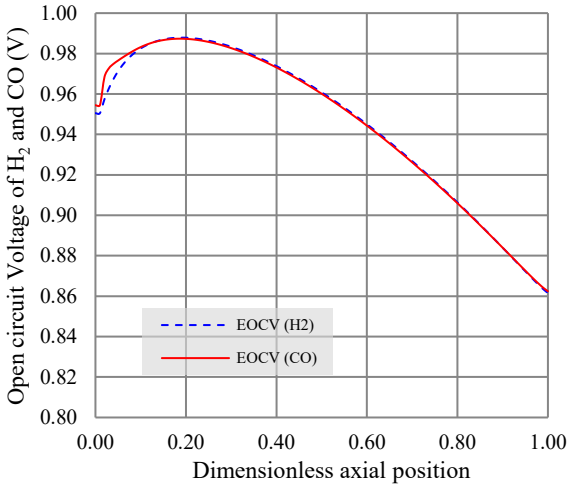

Fig. 18. Distribution of cell open circuit potentials associated with the CO and H2 electrochemical reactions.

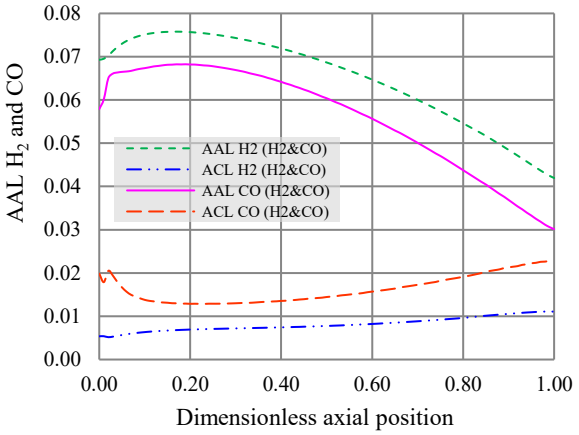

Fig. 19. Distribution of activation and concentration overpotentials associated with the CO and H2 electrochemical reactions.

4. Conclusions

A mathematical model of a quasi-two-dimensional model for a DIR-PSOFC supported by anode has been presented to solve the mass and energy conservation equations. The model incorporates an electrochemical model that evaluates the electric performance of the cell using the data obtained from the solution of conservation equations. The CO and H_2 electrochemical reactions, as well as the methane steam reforming reaction and the water-gas shift reaction, have been taken into account. The steady-state performance of the cell has been the subject of numerical investigation, with particular attention paid to the effect of

considering CO in the anode side TPB as a reactant on the temperature field, the distribution of gas constituents in the fuel channel, and the electric parameters of the cell. The following conclusions have been indicated:

1. If only H_2 is involved in the electrochemical reaction at the anode, the maximum power density is attained at a current density of 20400 A/m^2. At this point, the cell voltage is recorded at 0.416 V, while the power density has been measured to be 8313.04 W/m^2. It is noteworthy that the completely reformed fuel mixture was studied at 1073 K.
2. The cooling effect of the direct internal reforming reaction and its role in controlling the cell temperature gradient are clearly evident. The maximum temperature gradient of 146.98 K is observed in the PEN structure for a 10% pre-reformed fuel mixture at an average current density of 5000 A/m^2, operating at 1023 K. The fuel utilization and air ratio are set to 0.75 and 8.5, respectively, considering only the H_2 electrochemical reaction. The operating voltage was determined to be 0.65 V, the power density was calculated to be 3247 W/m^2, and the fuel efficiency was found to be 45.83%.
3. The findings indicate that CO accounts for no more than 20% of the total current density. The contribution of CO to the generation of electric current at the inlet is 15%, and at the point of maximum current density, it is 16.17%.
4. It has been demonstrated that incorporating CO as a reactant on the anode side TPB results in enhanced heat generation within the cell and facilitates elevated operating temperatures. It has been established that an elevated operating temperature will result in decreased activation and ohmic losses. This, in turn, will enhance both the local current density and the cell's operating voltage.
5. The incorporation of CO in both the electrochemical reaction and the WGSR results in a decline in the H_2 concentration and an augmentation in the H_2O concentration, in comparison to the scenario where solely H_2 is incorporated in the electrochemical reaction. The primary outcome of such variation in mole fractions is a decline in the (OCP) of the cell.
6. It has been demonstrated that the activation polarizations of the anode and cathode will decrease when the electrochemical reaction of CO is taken into consideration.
7. It has been demonstrated that the operating cell voltage increases from 0.68 V to 0.75 V under the consideration of CO as a reactant at the anode TPB. In addition, the power density has been shown to increase from 3411.396 W/m^2 to 3739.130 W/m^2. Furthermore, the fuel efficiency has been found to improve from 0.46 to 0.50 for a co-flow SOFC operating on a 30% pre-reformed fuel mixture at 1023 K, average current density of 5000 A/m^2, and fuel utilization and air ratios of 0.75 and 8.5, respectively.
8. It is found that the activation and concentration losses associated with the electrochemical oxidation of CO are less than those of H_2.

References

[1] S. C. Singhal, "*High Temperature SolidOxide Fuel Cells: Fundamentals, Design and Applications*." Oxford, UK: Elsevier Ltd, (2003).

[2] J. Larminie, A. Dicks, and M.S. McDonald, "*Fuel cell systems explained"*. Vol. 2, J. Wiley Chichester, UK, (2003).

[3] H. Khoshkam, K. Atashkari, and M. Borji, "Unsteady state numerical study of carbon deposition on the performance of solid oxide fuel cell and variation of porosity". *J. Compu. & Appl. Res. in Mech. Eng. (JCARME)*, Vol. 12, No. 2, pp. 247-261, (2023).

[4] C. O. Colpan, I. Dincer, and F. Hamdullahpur, "Thermodynamic modeling of direct internal reforming solid oxide fuel cells operating with syngas", *Int. J. Hydrogen Energy*, Vol. 32, No. 7, pp. 787-795, (2007).

[5] M. Andersson, J. Yuan, and B. Sundén, "SOFC modeling considering hydrogen and carbon monoxide as electrochemical reactants", *J. Power Sources*, Vol. 232: pp. 42-54, (2013).

[6] S. A. Hajimolana, M. A. Hussain, W. M. Ashri Wan Daud, M. Soroush and A. Shamiri, "Mathematical modeling of solid oxide fuel cells: A review", *Renew. Sustain. Energy Rev.*, Vol. 15, No. 4, pp. 1893-1917, (2015).

[7] N. Panwar, R. Kothari, and V. Tyagi, "Thermo chemical conversion of biomass–Eco friendly energy routes", *Renew. Sustain. Energy Rev.*, Vol. 16, No. 4, pp. 1801-1816, (2012).

[8] R. Toonssen, S. Sollai, P. V. Arvind, N. Woudstra, and A. H. M. Verkooijen, "Alternative system designs of biomass gasification SOFC/GT hybrid systems", *Int. J. Hydrogen Energy*, Vol. 36, No. 16, pp. 10414-10425, (2011).

[9] C. Bang-Møller and M. Rokni, "Thermodynamic performance study of biomass gasification, solid oxide fuel cell and micro gas turbine hybrid systems", *J. Energy Convers. Manag.*, Vol. 51, No. 11, pp. 2330-2339, (2010).

[10] S. Bedogni, S. Campanari, P. Iora, L. "Experimental analysis and modeling for a circular-planar type IT-SOFC", *J. Power Sources*, Vol.171, No. 2, pp. 617-625, (2007).

[11] K. Chen, Z. Lu, N. Ai, X. Chen, X. Huang and W. Su, "Experimental study on effect of compaction pressure on performance of SOFC anodes", *J. Power Sources*, Vol. 180, No. 1, pp. 301-308, (2008).

[12] S. Seidler, M. Henke, J. Kallo, W. G. Bessler, U. Maier and K. A. Friedrich, "Pressurized solid oxide fuel cells: Experimental studies and modeling", *J. Power Sources*, Vol. 196, No. 17, pp. 7195-7202, (2011).

[13] S. Kakac, A. Pramuanjaroenkij, and X.Y. Zhou, "A review of numerical modeling of solid oxide fuel cells", *Int. J. Hydrogen Energy*, Vol. 32, No. 7, pp. 761-786, (2007).

[14] H. Hesami, M. Borji, and J. Rezapour, "Three-dimensional numerical investigation on the effect of interconnect design on the performance of internal reforming planar solid oxide fuel cell", *Korean J. Chem. Eng.*, Vol. 38, No. 12, pp. 2423-2435, (2021).

[15] H. Hesami, M. Borji, and J. Rezapour, "A comprehensive three-dimensional modeling of an internal reforming planar solid oxide fuel cell with different interconnect designs", *J. Solid State Electrochem.*, Vol. 25, No. 10, pp. 2639-2664, (2021).

[16] A. Ashar, Y. Gu, G. Jackson, R. Braun, "Achieving high power density in SOFCs for transportation applications: A model-based assessment of YSZ- and GDC-based electrolyte architectures". *J. Energy Convers. Manag.*, Vol. 348, Part B, pp. 120661, (2026).

[17] F. Peng, H. Li, W. Liu, Q. Zhu, "Multiphysics modeling and deep learning-driven multi-objective optimization of the oxygen electrode microstructure in solid oxide electrolysis cell considering oxygen distribution uniformity and residual stress-induced failure". *J. Energy Convers. Manag.,* Vol. 348, Part A, pp. 120648, (2026).

[18] M. L. Ferrari, "Solid oxide fuel cell hybrid system: control strategy for stand-alone configurations". *J. Power Sources*, Vol. 195, No.3, pp. 685-7, (2010).

[19] F. Zabihian, and A.S. Fung, "Performance analysis of hybrid solid oxide fuel cell and gas turbine cycle (part I): Effects of fuel composition on output power", *J. Energy Inst.*, Vol. 87, No. 1, pp. 18-27, (2014).

[20] H. Ozcan, and I. Dincer, "Performance evaluation of an SOFC based trigeneration system using various gaseous fuels from biomass gasification", *Int. J. Hydrogen Energy*, Vol. 40, No. 24, pp. 7798-7807, (2015).

[21] M. Hatef, E. Golamian, S.M. Seyed Mahmoudi, Ali Saber Mehr, "Enhancing efficiency and reduced CO2 emision in hybrid biomass gasification with integrated SOFC-MCFC system based on CO2 recycle". *J. Energy Convers. Manag.*, Vol. 313, pp. 118611, (2024).

[22] X. Zhou, W. Chen, B. Zhang, "Proposed hybrid system with integrated SOFC, gas turbine, and compressor-assisted absorption refrigerator using [mmim]DMP/CH3OH as working fluid". *J. Energy*, Vol. 261, Part B, pp. 125301, (2022).

[23] Z. Wang, X. Yang, J. Xu, X. Wang, F. Deng, Z. Huang, "Scheduling of integrated energy system considering the combined operation of SOFC and dynamic hydrogen-blended gas turbine. ", *Int. J. Hydrogen Energy*, Vol. 190, pp. 152221, (2025).

[24] P. Aguiar, D. Chadwick, and L. Kershenbaum, "Modelling of an indirect internal reforming solid oxide fuel cell", *Chem. Eng. Sci.*, Vol. 57, No. 10, pp. 1665-1677, (2002).

[25] P. Aguiar, C.S. Adjiman, and N.P. Brandon, "Anode-supported intermediate temperature direct internal reforming solid oxide fuel cell. I: model-based steady-state performance", *J. Power Sources*, Vol. 138, No. 1-2, pp. 120-136, (2004).

[26] O. Corigliano, G. Florio, and P. Fragiacomo, "A numerical simulation model of high temperature fuel cells fed by

biogas", *Energy Sources, Part A*, Vol. 34, No. 2, pp. 101-110, (2011).
[27] M. A. Abdelkareem, W. H. Tanveer, E. T. Sayed, M. E. H. Asad, A. Allagui and S. W. Cha, "On the technical challenges affecting the performance of direct internal reforming biogas solid oxide fuel cells" *Renew. Sustain. Energy Rev.*, Vol. 101, pp. 361-375, (2019).
[28] E. Achenbach, "Three-dimensional and time-dependent simulation of a planar solid oxide fuel cell stack", *J. Power Sources*, Vol. 49, No. (1-3), pp. 333-348, (1994).
[29] H. Iwai, H., Y. Yamamoto, M. Saito and H. Yoshida, "Numerical simulation of intermediate-temperature direct-internal-reforming planar solid oxide fuel cell", *J. Energy*, Vol. 36, No. 4, pp. 2225-2234, (2011).
https://doi.org/10.1016/j.energy.2010.03.058
[30] J. J. Ramírez-Minguela, V. H. Rangel-Hernandez, J. A. Alfaro-Ayala, A. R. Uribe-Ramirez, J. M. Mendoza-Miranda, J. M. Belman-Flores and B. Ruiz-Camacho, "Energy and entropy study of a SOFC using biogas from different sources considering internal reforming of methane", *Int. J. Heat Mass Trans.*, Vol. 120, pp. 1044-1054, (2018).
[31] A. Burt, I. B. Celik, R. S. Gemmen and A. V. Smirnov, "A numerical study of cell-to-cell variations in a SOFC stack", *J. Power Sources*, Vol. 126, No. 1-2, pp. 76-87, (2004).
[32] M. Iwata, T. Hikosaka, M. Morita, T. Iwanari, K. Ito, K. Ondo, Y. Esaki, Y. Sakaki and S. Nagata, "Performance analysis of planar-type unit SOFC considering current and temperature distributions", *Solid State Io*n., Vol. 132, No. 3-4, pp. 297-308, (2000).
[33] S. Nagata, A. Momma, T. Kato and Y. Kasuga, "Numerical analysis of output characteristics of tubular SOFC with internal reformer", *J. Power Sources*, Vol. 101, No. 1, pp. 60-71, (2001).
[34] P. Aguiar, C. Adjiman, and N. Brandon, "Anode-supported intermediate-temperature direct internal reforming solid oxide fuel cell: II. Model-based dynamic performance and control", *J. Power Sources*, Vol. 147, No. 1-2, pp. 136-147, (2005).
[35] H. Yakabe, T. Ogiwara, M. Hishinuma and I. Yasuda, "3-D model calculation for planar SOFC", *J. Power Sources*, Vol. 102, No. 1-2, pp. 144-154, (2001).
[36] D. Bhattacharyya, R. Rengaswamy, and C. Finnerty, "Isothermal models for anode-supported tubular solid oxide fuel cells", *Chem. Eng. Sci.*, Vol. 62, No. 16, pp. 4250-4267, (2007).
[37] M. Borji, K. Atashkari, N. Nzadeh and M. Masoumpour, "Modeling, parametric analysis and optimization of an anode-supported planar solid oxide fuel cell", *Proc. Inst. Mech. Eng. C. J. Mech. Eng. Sci.,* Vol. 229, No. 17, pp. 3125-3140, (2015).
[38] R. Suwanwarangkul, E. Croiset, E. Entchev, S. Charojrochkul, M. D. Pritzker, M. W. Fower, P. L. Douglas, S. Chewathanakup and H. Mahaudom, "Experimental and modeling study of solid oxide fuel cell operating with syngas fuel", *J. Power Sources*, Vol. 161, No. 1, pp. 308-322, (2006).
[39] C. Stiller, *"Design, operation and control modelling of SOFC/GT hybrid systems*", Norwegian University of Science and Technology (NTNU), Norway, (2006).
[40] S. Chan, S., K. Khor, and Z. Xia, "A complete polarization model of a solid oxide fuel cell and its sensitivity to the change of cell component thickness", *J. Power Sources*, Vol. 93, No. 1-2, pp. 130-140, (2001).
[41] B. E. Poling, J.M. Prausnitz, and J.P. O'connell, "*The properties of gases and liquids"*, 5th ed., Mcgraw-hill New York, (2001).